High-Temperature Stability Amorphous Ternary AlBN Dielectric Films on N ++ GaN

Fengfeng Liu, Yuxiong Li, Xavier Devaux, Yuan Lu, Yi Luo, Zhanpeng Sui, Yong Cai, Chunping Jiang

Adv. Eng. Mater. 2022, 2200191 DOI: 10.1002/adem.202200191

High-Temperature Stability Amorphous Ternary AlBN Dielectric Films on $N^{++}GaN$

Fengfeng Liu, Yuxiong Li, Xavier Devaux, Yuan Lu, Yi Luo, Zhanpeng Sui, Yong Cai, Chunping Jiang**

F. F. Liu, Y. X. Li, Y. Cai, C. P. Jiang
School of Nano-Tech and Nano-Bionics, University of Science and Technology of China, Hefei 230026, China
E-mail: cpjiang2008@sinano.ac.cn
F. F. Liu, Y. X. Li, Z. P. Sui, Y. Cai, C. P. Jiang
Key Lab of Nanodevices and Applications, Suzhou Institute of Nano-Tech and Nano-Bionics, Chinese Academy of Sciences, Suzhou 215123, China
X. Devaux, Y. Lu
Institut Jean Lamour, UMR 7198, CNRS-Université de Lorraine, Campus ARTEM, 2 allée André Guinier, 54011 Nancy Cedex, France
Y. Luo
Micro/Nano Fabrication Laboratory, Microsystem & Terahertz Research Center, Chengdu, 610200, China
E-mail: luoyi@mtrc.ac.cn

Keywords: AlBN, high-temperature stability, amorphous dielectric films, pulsed laser deposition

Dielectric films have played a vital role in the development of micro- and nano-electronic devices over the past decades. However, the stability of current dielectrics under extreme high-temperature conditions is still a major shortcoming to be overcome. Herein, we report the successful fabrication of high-quality amorphous ternary AlBN dielectric films on $n^{++}GaN$ substrates by pulsed laser deposition (PLD) at room temperature (25±2 ℃). Systematic characterizations on the morphology, structure, chemical composition, and band offsets properties of the fabricated films revealed that both as-deposited and 800 ℃ post-deposition annealing (PDA) thin films were amorphous and exhibited good physical and electrical properties. Large band offsets (>2.0 eV), high dielectric constants (>10), and low leakage currents were achieved in both cases. Furthermore, the leakage current density in the Au/AlBN/$n^{++}GaN$ junctions of 800 ℃ PDA thin films was reduced by approximately one order of magnitude compared to those of as-deposited thin films. The demonstration of these excellent properties indicate that the amorphous AlBN dielectric thin films are promising candidates for integrated dielectric layers in electronic devices for harsh environment applications.

1. Introduction

Considering the increasing demand for high current density, breakdown field, frequency, and temperature operation performance in III-nitride electronic devices, ensuring the high-temperature stability and reliability of dielectric films has become more challenging.[1-4] For high electron mobility transistors, inserting a dielectric film under gate metal or depositing the passivation with dielectrics on the gate-drain access region effectively reduces gate leakage, enlarges gate swing, and suppresses current collapse, which improves the device performance significantly.[5] Various binary metal oxide/nitride dielectrics, such as SiO_2,[6] Si_3N_4,[7] Al_2O_3,[8] HfO_2,[9] MgO,[10] Sc_2O_3,[11] Ta_2O_5,[12] ZrO_2,[13] BN,[14, 15] and AlN,[16, 17] have been fabricated by physical or chemical vapor deposition methods. Although conventional SiO_2, Si_3N_4, and Al_2O_3 have good high-temperature stability, their dielectric constant (κ) values are relatively low ($\kappa < 10$). Furthermore, the equivalent oxide thickness is low, which cannot meet the demand for devices with high voltage and frequency. Although several oxide dielectric films with low crystallization temperatures of 400–500 °C, such as HfO_2 and ZrO_2, have higher κ values (typically larger than 10), they are generally less stable at high temperatures.[18] Moreover, annealing at a temperature higher than 800 °C is still the typical process employed for fabricating ohmic electrodes on III-N semiconductors.[19, 20] In addition, the local heat-flow power density in the region near the junction for GaN transistors could exceed 30 W/mm,[21, 22] resulting in the failure of these devices.[23] When these oxide dielectric films (usually grown at room temperature or low temperatures in the range of 200–400 °C) undergo high-temperature processing during device preparation or operate in environments with extremely high temperature, they may recrystallize, resulting in a large number of grain boundaries or defects and thus forming leakage channels. Consequently, an increase in the leakage current during the operation degrades the electrical properties of such devices.[24] Recently, two-dimensional semiconductor dielectric materials, such as hexagonal boron nitride (h-BN), have attracted great

attention owing to their extraordinary properties.[25] However, the current method to synthesize large-size and high-quality h-BN involves chemical vapor deposition at high temperatures. In addition, the transfer of h-BN to another suitable substrate may introduce mechanical deformations and chemical impurities on the h-BN surface, creating many inconveniences and uncertainties for the preparation of device and its applications.[26, 27] AlN dielectric film has gained immense recognition in III-N electronic devices because of its superior properties such as high thermal conductivity (320 $W \cdot m^{-1} \cdot °C^{-1}$ at 25 °C), large bandgap (E_g=6.2 eV), low thermal expansion coefficient (4.5×10^{-6} $°C^{-1}$), and high melting point (approximately 2400 °C). However, many studies have shown that amorphous AlN films could contain nano-sized AlN grains during film growth, which could grow during the high-temperature post-treatment process.[28-30] Nevertheless, introducing an appropriate type of doping element and approximate number of dopant atoms into the amorphous dielectric films is an effective method to suppress the formation of nanograins and simultaneously, improve the crystallization temperature to a greater extent.[31-33] Thus, doping the atoms has offered a powerful approach to achieving high-temperature stability in dielectric films. However, the modification of AlN dielectric films to eliminate the influence of nanograins remains unexplored, which is particularly important for III-N semiconductor devices.

Herein, we report the fabrication of novel amorphous ternary AlBN dielectric films on heavily doped n^{++}GaN (0002) substrates at room temperature by the pulsed laser deposition technique. We introduced boron (B) atoms, having the smallest radius in the group III, into the amorphous AlN film. The relatively large difference between the atomic radii of B and Al effectively disrupted the periodic arrangement of Al–N to form an amorphous structure with stronger phase stability compared to that of the binary metal nitrides. Subsequently, we systematically investigated the structure, energy band alignment, and electrical properties of the as-deposited and 800 °C post-deposition annealing (PDA) AlBN films. The microstructure of the films was characterized by atomic force microscope (AFM), X-ray diffraction (XRD), and high-

resolution transmission electron microscopy (HR-TEM). The energy band alignment of the as-deposited and 800 ℃ PDA AlBN/GaN was studied using X-ray photoelectron spectroscopy (XPS). Finally, the electrical and dielectric properties of the as-deposited and 800 ℃ PDA AlBN films were analyzed using simple Au/AlBN/n^{++}GaN junctions; the results suggest good dielectric properties of this new type of ternary film and demonstrate an excellent dielectric layer candidate in III-N semiconductor devices.

2. Results and Discussion

All AlBN films were grown by pulsed laser deposition (PLD) on n^{++}GaN (0002) substrates (resistivity $\leq 6.0\times10^{-3}$ Ω·cm) at room temperature. **Figures 1**a and b show the surface morphologies of the as-deposited and 800 ℃ PDA AlBN films, demonstrating flat surfaces. The root-mean-square (RMS) surface roughness was 0.429 nm and 0.428 nm in 1×1 μm^2 surface, respectively, indicating that the high-temperature annealing had almost no effect on the surface morphology of the films.

Figure 1c illustrates the crystalline structure of the films analyzed by XRD in the 2θ range of 20° to 90°. Except for the diffraction peak corresponding to the GaN substrates, no sharp Bragg peaks were observed for the as-deposited and 800 ℃ PDA films, indicating the possible amorphous structure of the fabricated films. However, because the (0002) diffraction peaks of hexagonal GaN and hexagonal AlBN are theoretically close, their weak diffraction peaks may be hidden by the strong diffraction of GaN (0002) considering that a small amount of AlBN grains are present in the films. Therefore, to determine the presence of grains with poor crystallinity in the films, the cross-sectional AlBN samples of the as-deposited and 800 ℃ PDA films were characterized by HR-TEM and electron energy-loss spectrometry (EELS).

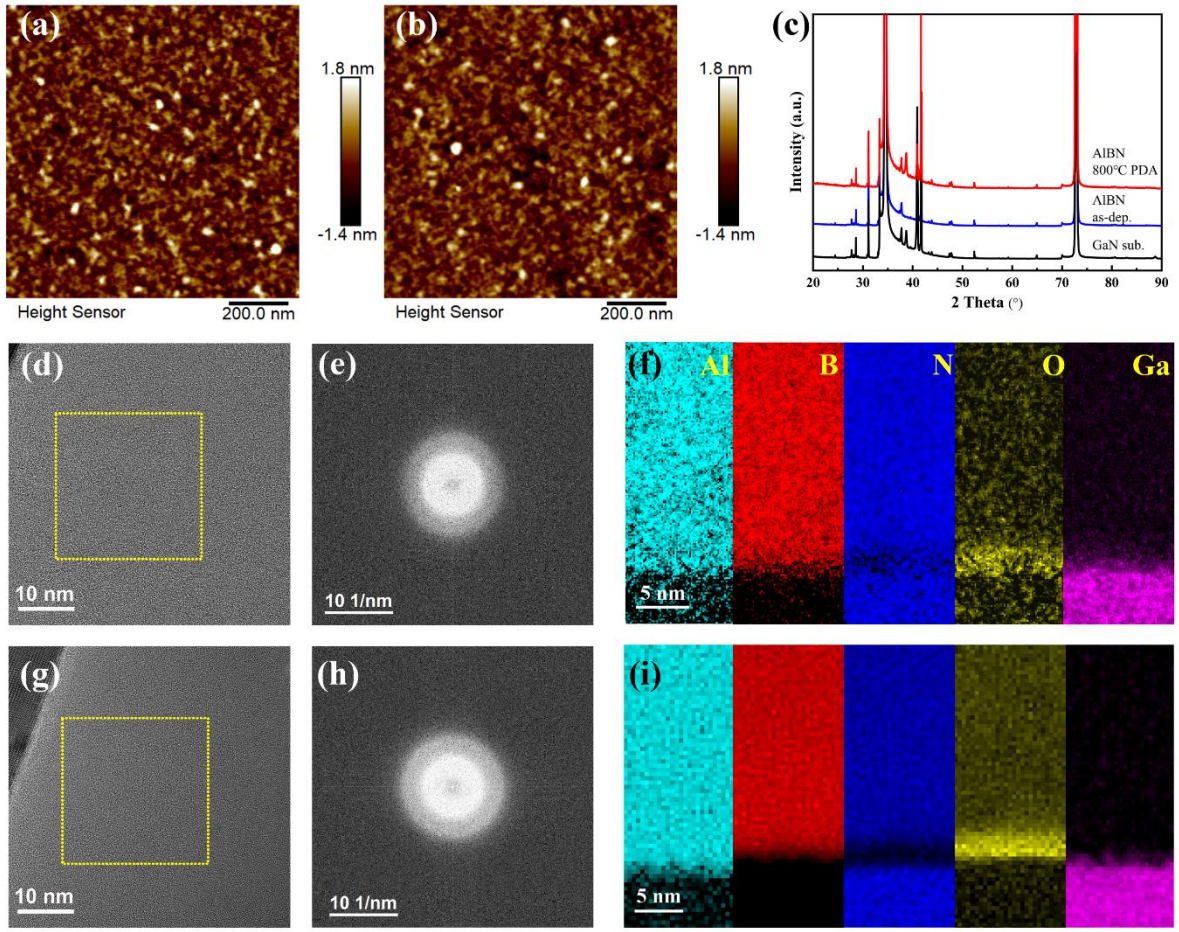

Figure 1. The atomic force microscope images of the surface of the a) as-deposited and b) 800 ℃ PDA films. c) The X-ray diffraction patterns of the GaN substrate, as-deposited, and 800 ℃ PDA AlBN films on GaN (0002). The cross-sectional high-resolution transmission electron microscopy images of the d) as-deposited and g) 800 ℃ PDA films. e) and h) The fast Fourier transform results of the e) as-deposited and h) 800 ℃ PDA films in the yellow domain of d) and g), respectively. The EELS mappings of the f) as-deposited and i) 800 ℃ PDA films.

As observed in Figures 1d and g, the atoms in the as-deposited and 800 ℃ PDA AlBN films are randomly arranged. Each corresponding fast Fourier transform (FFT) image exhibits diffuse rings, further confirming that the AlBN films maintain a single amorphous form in the as-deposited and 800 ℃ PDA AlBN films. The elemental distributions of Al, B, N, O, and Ga at the AlBN/GaN interface in the as-deposited and 800 ℃ PDA films were characterized by EELS, as shown in Figures 1f and i. The Al, B, and N atoms were uniformly distributed without segregation and agglomeration in both the films. In addition, a certain amount of O was observed in the entire EELS scanned profile, particularly in the AlBN layers and at AlBN/GaN interfaces. This observation could be attributed to the existence of oxygen impurities in the

prepared AlBN films, the surface of the GaN substrates used, or the oxidative contamination of the thin TEM lamella.

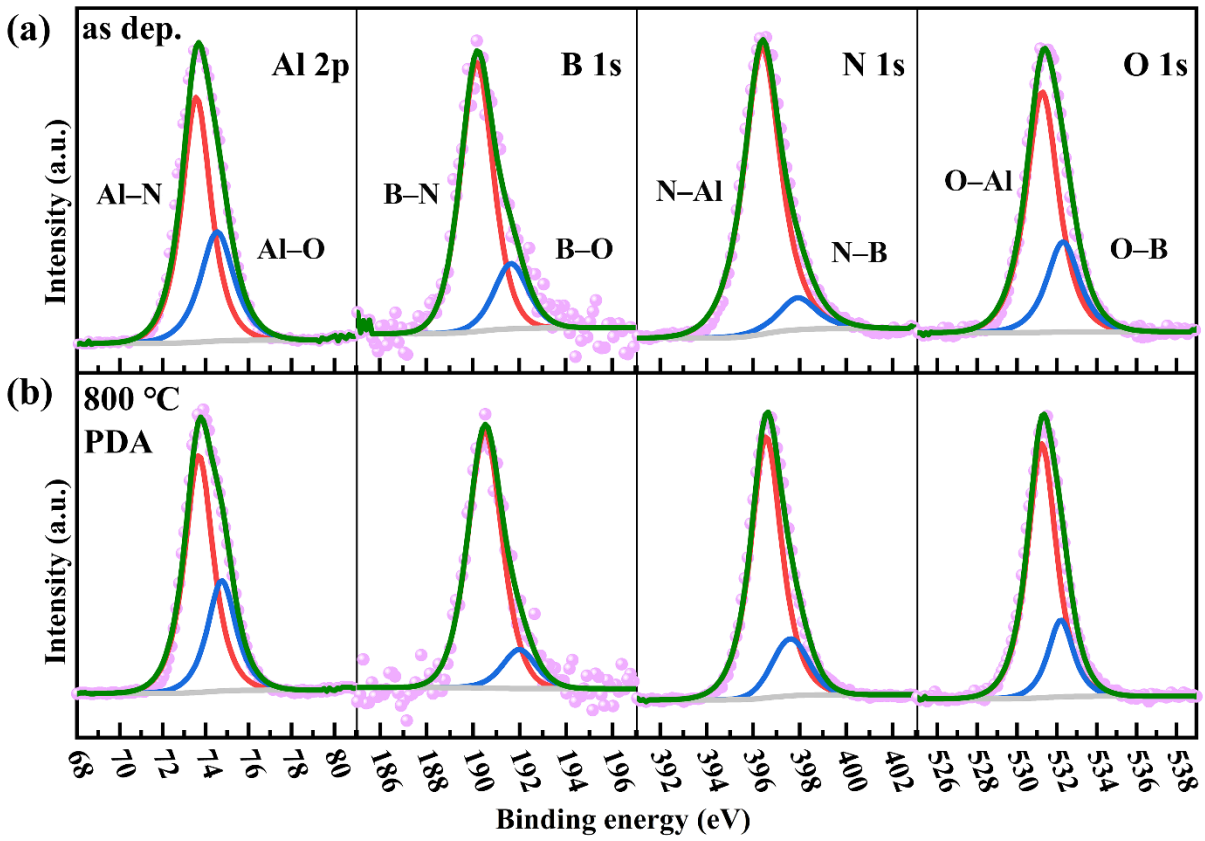

Figure 2. The X-ray photoelectron spectroscopy profiles of AlBN films after cleaning using Ar^+ sputtering for 1 min. a) as-deposited and b) 800 °C PDA films.

The bulk AlBN films were further characterized by XPS to obtain more quantitative information on the chemical bonding and composition. **Figure 2** illustrates the Al 2p, B 1s, N 1s, and O 1s core-level (CL) spectra for the as-deposited and 800 °C PDA samples and the deconvolution fitting of spectra. The deconvoluted peaks allow the identification of different chemical states of elements. The binding energies of all spectra were referenced to the C 1s signal of the adventitious carbon, which was set to 284.8 eV. The relative components in the as-deposited and 800 °C PDA samples and the type of valence bond between the elements were almost unchanged. The ratio of Al:B:N was approximately 5.0:1.0:5.1 for the as-deposited and 800 °C PDA samples, as determined by the XPS quantitative analysis using calibrated atomic sensitivity factors. The result suggested that the component of AlBN films were unchanged

after the high-temperature PDA process. The following two distinct chemical states were observed for the Al 2p binding: the Al 2p#1 and Al 2p#2 subpeaks at approximately 73.5 and 74.5 eV, corresponding to the Al–N and Al–O bonds, respectively. The relative area of the Al–N and Al–O peaks were unchanged in the as-deposited and 800 ℃ PDA samples, indicating that the content was stable during the PDA process under N_2 atmosphere. The B 1s XPS profile was fitted by two subpeaks located at approximately 190.2 and 191.7 eV, corresponding to the B–N and B–O bonds, respectively. The intensity of the B–O peak decreased while that of the B–N peak increased after PDA at 800 ℃, implying that the B–O component was partially transformed into B–N component after annealing. The N 1s spectra could also be fitted into two subpeaks located at approximately 396.4 and 397.9 eV, which were assigned to the N–Al and N–B bonds, respectively. The intensity of the N–B peak increased after annealing, which was consistent with the obtained result of the B–N peak. In addition, XPS measurements of the as-deposited AlBN film after 4 min of Ar^+ sputtering cleaning suggested that the oxygen and carbon contents in the film were approximately 4.81% and 0.71% (**Figure S1,** Supporting Information), respectively. This result could be ascribed to the impurities in the Al–B–N target used in the PLD preparation or the Ar^+ etching process.

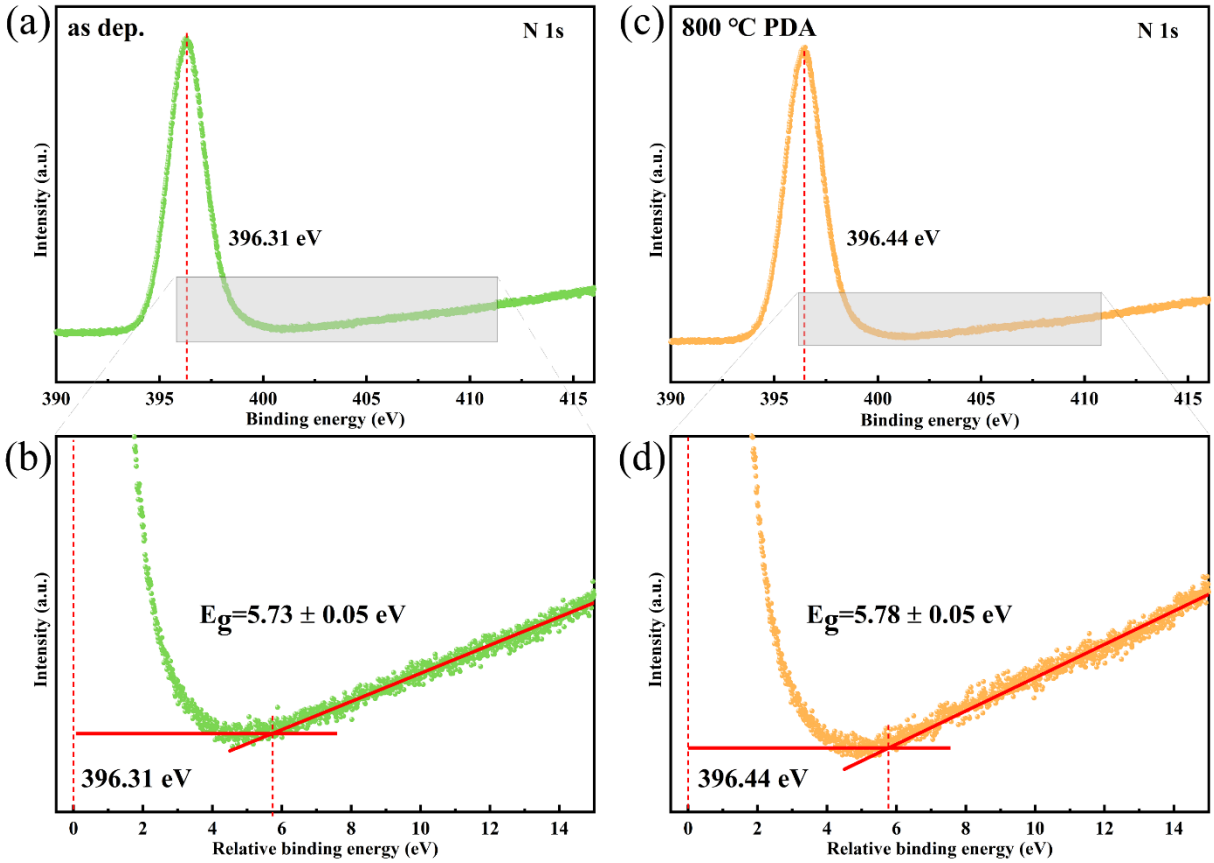

Figure 3. The N 1s core-level spectrum of the a) as-deposited and b) 800 °C PDA AlBN samples; c) and d) the magnified illustrations of the inelastic background region marked in figures a) and c), respectively. The distance from the onset of the inelastic background to the location of the N 1s core level is determined by the linear extrapolation from the red marker, corresponding to the film bandgap.

For GaN-based metal–insulator–semiconductor (MIS) gate structures, the leakage current can be well suppressed when the conduction band offset (ΔE_c) of metal/dielectric and semiconductor/dielectric are sufficient. From experiences in complementary metal–oxide–semiconductor (COMS) technology, the tunneling leakage current can be well controlled when the conduction band offset is larger than 1.0 eV.[34] In the present study, the bandgap of films was obtained from XPS measurements by analyzing the onset of the inelastic background at the high binding energy side of a strong CL peak. The N 1s CL spectra of the as-deposited and 800 °C PDA AlBN samples are illustrated in **Figures 3**a and c, respectively. The strongest signals of the as-deposited and 800 °C PDA samples correspond to the primary photoelectron peaks located at the binding energy of 396.31 and 396.44 eV, respectively. Figures 3b and d

demonstrate the enlarged background regions of the N 1s CL spectra, as indicated by the gray boxes in Figure 3a and c. The x-axes in Figures 3b and d are relative binding energies with respect to the N 1s peak position of each sample. Linear extrapolation was applied to the measured inelastic loss spectra curve near the approximate location of the onset of inelastic losses. The bandgap energy was equal to the difference between the CL peak energy and the onset of inelastic losses. The bandgap of AlBN was 5.78±0.05 eV of 800 ℃ PDA film, which was in agreement with that of the as-deposited AlBN (5.73±0.05 eV) within the allowed error range.[35] These results are consistent with the values determined from transmission spectroscopy (**Figures S2** and **S3,** Supporting Information).

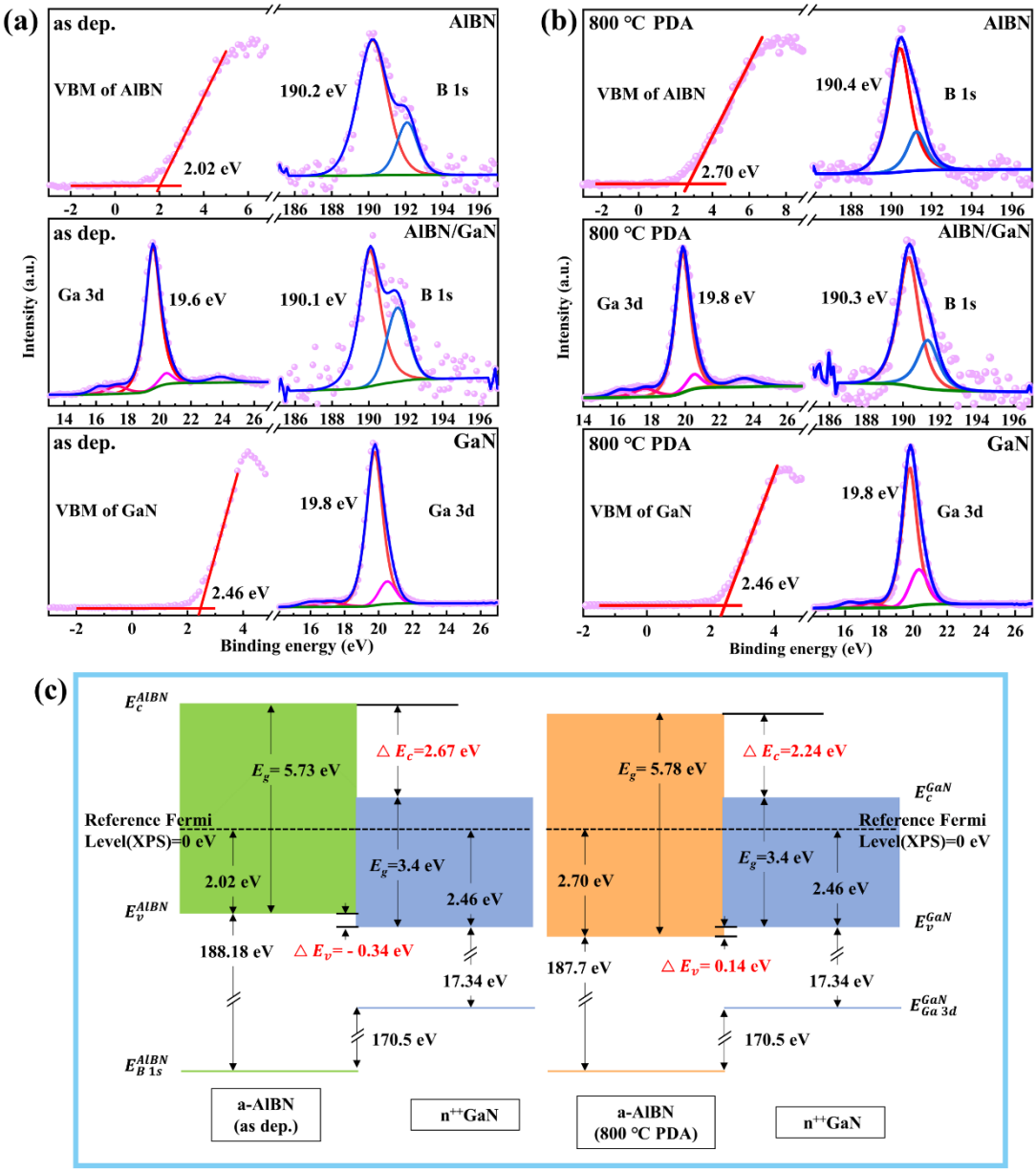

Figure 4. Figures a) and b) represent the valence band spectrum and B 1s core level of the as-deposited and 800 °C PDA AlBN films, the Ga 3d and B 1s core levels of the as-deposited and 800 °C PDA AlBN/GaN samples, and the valence band spectrum and Ga 3d core level of the unannealed and 800 °C-annealed GaN substrates. c) The energy band diagrams of AlBN/GaN based on the X-ray photoelectron spectroscopy results.

The valence band offset (ΔE_v) at the heterostructure interface was determined using the CL photoemission-based Kraut method. The ΔE_v of the AlBN/GaN heterojunction is calculated as follows:[36, 37]

$$\triangle E_V = \left(E_{Ga3d}^{AlBN/GaN} - E_{B1s}^{AlBN/GaN}\right)_{AlBN/GaN} + \left(E_{B1s}^{AlBN} - E_{VBM}^{AlBN}\right)_{\text{bulk, AlBN}} - (E_{Ga3d}^{GaN} - E_{VBM}^{GaN})_{\text{bulk, GaN}}$$

(1)where $\left(E_{Ga3d}^{AlBN/GaN} - E_{B1s}^{AlBN/GaN}\right)_{AlBN/GaN}$ is the energy difference between the Ga 3d and B 1s CLs, which are measured in the AlBN/GaN interface samples (AlBN layers thickness are approximately 5 nm). $\left(E_{B1s}^{AlBN} - E_{VBM}^{AlBN}\right)_{\text{bulk, AlBN}}$ and $(E_{Ga3d}^{GaN} - E_{VBM}^{GaN})_{\text{bulk, GaN}}$ are the energy differences of the CLs and valence band maximum (VBM) binding energy in the bulk AlBN samples (thickness approximately 70 nm) and GaN substrates (thickness approximately 5 μm), respectively. **Figures 4**a and b illustrate the valence band, B 1s, and Ga 3d CL spectra of the as-deposited and 800 ℃ PDA samples. The Ar ion cleaning was not performed on the six samples of the as-deposited or 800 ℃ PDA prior to the XPS measurements. The binding energies were referenced to the C 1s binding energy of the adventitious carbon contamination, which was considered 284.8 eV. The CL positions were determined after the Shirley-background correction and fitting with Gaussian–Lorentzian peaks. Moreover, the locations of the VBM are obtained by the linear extrapolation of the valence band leading edge to the background of spectra, as shown in Figures 4a and b. The binding energies for E_{VBM}^{AlBN} of the as-deposited and 800 ℃ PDA AlBN bulk films are located at 2.02 and 2.70 eV, respectively, as indicated by the red lines. The values of $\left(E_{B1s}^{AlBN} - E_{VBM}^{AlBN}\right)_{\text{bulk, AlBN}}$ for the as-deposited and 800 ℃ PDA AlBN bulk films were 188.18±0.05 eV and 187.70±0.05 eV, respectively, which were calculated by measuring the difference between B 1s and VBM. The values of $\left(E_{Ga3d}^{AlBN/GaN} - E_{B1s}^{AlBN/GaN}\right)_{AlBN/GaN}$ were 170.5 eV for both the as-deposited and 800 ℃ PDA AlBN/GaN interface samples. Similar annealing procedure was performed for the cleaned GaN substrate. The E_{VBM}^{GaN} in the XPS profile of the Ga 3d CL was unchanged after annealing owing to the high stability of the bulk GaN substrate at high

temperatures; the values of $(E_{Ga3d}^{GaN} - E_{VBM}^{GaN})_{\text{bulk, GaN}}$ was 17.34±0.05 eV. The as-deposited and 800 ℃ PDA valence band offsets were -0.34±0.05 eV and 0.14±0.05 eV, respectively, which were obtained by substituting the $\left(E_{Ga3d}^{AlBN/GaN} - E_{B1s}^{AlBN/GaN}\right)_{AlBN/GaN}$, $(E_{B1s}^{AlBN} - E_{VBM}^{AlBN})_{\text{bulk, AlBN}}$ and $(E_{Ga3d}^{GaN} - E_{VBM}^{GaN})_{\text{bulk, GaN}}$ values in Eq. (1). A negative value indicated that the VBM level of AlBN was lower than that of GaN. Subsequently, the ΔE_c is determined by the following equation:[37]

$$\triangle E_c = E_g^{AlBN} - E_g^{GaN} - \triangle E_V \quad (2)$$

where E_g^{AlBN} and E_g^{GaN} are the bandgaps of AlBN and GaN (3.4 eV), respectively. Using the determined bandgaps of AlBN, the calculated value of ΔE_c was 2.67±0.05 and 2.24±0.05 eV for the as-deposited and 800 ℃ PDA samples, respectively. The schematic band diagram of the as-deposited and 800 ℃ PDA AlBN/GaN structures is shown in Figure 4c. The measured values of ΔE_c exceeded 2.0 eV for the as-deposited and 800 ℃ PDA samples, which was greater than 1.0 eV, providing excellent electron confinement and blocking effect. Based on the XPS results, the band alignment transition of AlBN/GaN interfaces from type II to type I occurred before and after annealing at 800 ℃. This observation may arise from the reduction of negative charges of oxygen-rich bonds in the AlBN films or the interdiffusion of AlBN/GaN interface after PDA. In addition, the gap between the Fermi level and the valence band maximum of 800 ℃ PDA AlBN/GaN sample was larger than that of the as-deposited sample, indicating better insulating properties of PDA AlBN film and stronger suppression of the minority carrier (hole) current in the junction.

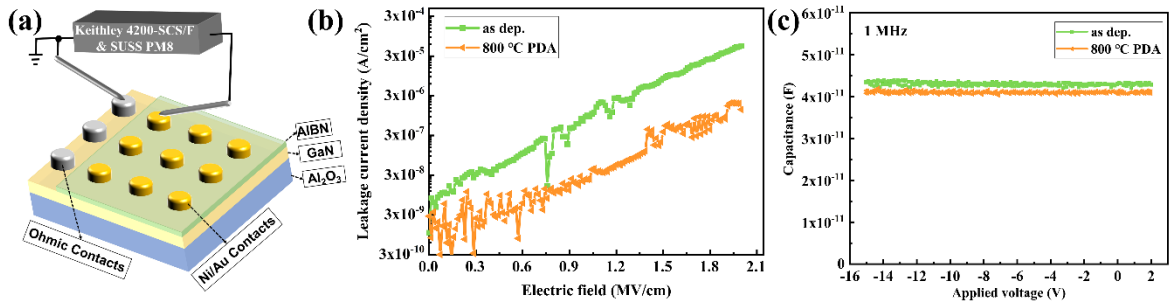

Figure 5. a) The structure diagram of Au/AlBN/n^{++}GaN capacitors. b) Current density–electric field (J–E) characteristics of AlBN thin films and c) the capacitance–voltage (C–V) characteristics of AlBN Au/AlBN/n^{++}GaN capacitors at a frequency of 1 MHz.

To further verify the electrical and dielectric properties of the as-deposited and 800 °C PDA samples, simple Au/AlBN (thickness approximately 70 nm)/n^{++}GaN capacitors have been fabricated, as shown in **Figure 5**a. Au and n^{++}GaN were adopted as the top and bottom electrodes, respectively. The leakage current characteristics of the as-deposited and 800 °C PDA dielectric films are illustrated in Figure 5b. The leakage current of the as-deposited film increased with the increasing electric field and reached 5.6×10^{-5} A/cm^2 at 2 MV/cm, indicating that the as-deposited AlBN films exhibited superior insulating characteristics.[38-40] The leakage current density of 800 °C PDA sample was approximately one order of magnitude lower than that of the as-deposited sample. The improved electrical properties of the 800 °C PDA sample could be attributed to the following two reasons: First, the positive valence band offset after the high-temperature treatment reduced the possibility of hole injection. Second, the atoms could rearrange during the high-temperature annealing process. The density of the nitrogen vacancies and micropores decreased while that of the AlBN film increased, resulting in decreased leakage channels. Moreover, the dependence of the capacitance on the applied voltage of both samples is measured, as shown in Figure 5c; the area of the capacitors used for the measurements was 3.14×10^4 μm^2. The measurements were conducted with minimum three junctions for each sample. The capacitance–voltage (C–V) curves did not demonstrate hysteresis or depletion behaviors as compared to the typical MIS capacitance structure. However, the capacitance values were almost constant from -15 to 2 V. Considering that the substrate was heavily doped

n^{++}GaN (resistivity ≤ 6.0×10^{-3} Ω·cm), it possessed good conductivity comparable to that of a metal and therefore acted as a metal electrode. The relative dielectric constant (κ) can be evaluated by the following relation:[41, 42]

$$\kappa = \frac{Cd}{\varepsilon_0 A} \quad (3)$$

where d is the AlBN films thickness, ε_0 is the dielectric constant of vacuum, and A represents the area. The calculated κ values of the as-deposited and 800 ℃ PDA AlBN films are 10.80 and 10.32 at 1 MHz, respectively, which are higher than that of the conventional SiO_2, Si_3N_4, and Al_2O_3 (3.9, 7, and 9, respectively) dielectric materials. This result implies that the amorphous AlBN films have good high-κ dielectric characteristics for high-performance electronics.

3. Conclusion

In summary, high-quality amorphous AlBN dielectric thin films were successfully fabricated at room temperature by PLD. The fabricated films exhibited stable amorphous structures with no crystallization and degradation up to 800 ℃ of annealing. Good physical and electrical properties such as large band offsets (>2.0 eV), high dielectric constants (>10), and low leakage currents were also achieved in both the as-deposited and 800 ℃ PDA AlBN films. Moreover, the leakage current density of the 800 ℃ PDA AlBN film was one order of magnitude lower than that of the as-deposited AlBN film. All the results show that this new type of high-temperature stable dielectric film is a promising candidate for high-temperature, high-frequency, and high-power applications in III-N semiconductor devices.

4. Experimental Section

Preparation of N^{++}GaN Substrates: In this study, a 4.5±0.5 μm-thick silicon (Si)-doped c-plane GaN layer (resistivity ≤ 6.0×10^{-3} Ω·cm, donor density > 1×10^{18} cm^{-3}) was adopted. It was grown by hydride vapor phase epitaxy on a 430±25 μm-thick sapphire substrate by the Suzhou Nanowin Science and Technology Co., Ltd (China). The n^{++}GaN-on-sapphire (n^{++}GaN

substrate, Suzhou Nanowin Science and Technology Co., Ltd., China) had a nominal dislocation density below 5×10^{8} cm^{-2} and was chemomechanically polished on a single side. Prior to the PLD processing, each n^{++}GaN substrate was cut into 10×10 mm^2 pieces. A wet chemical cleaning process was applied to the n^{++}GaN substrates, which included sonicating in acetone and isopropyl alcohol individually for 20 min at room temperature, and a buffered oxide etchant (49% HF:40% NH_4F = 1:7 vol.%) solution for 1 min at room temperature to remove surface native oxides.

Thin-Film Preparation: Amorphous AlBN dielectric films were deposited by the PLD technique. A KrF gas excimer laser emitting at a wavelength of 248 nm (COHERENT, COMPexPro201) was adopted with pulse width of 25 ns. A ceramic target (AlN:BN=8:2 at.%) was placed parallel to substrate at a distance of 60 mm. The high-vacuum chamber was pumped down to a background pressure of approximately 10^{-7} Pa. The rotation of carousels throughout the deposition was kept constant at 10 revolutions per minute. The laser beam energy and pulse repetition rate were set at 350 mJ and 2 Hz, respectively, during deposition; the substrate was not heated intentionally. The deposition of the AlBN thin films was performed in high-purity nitrogen (99.999%) ambient at a pressure of 0.5 Pa.

800 ℃ Post-Deposition Annealing (PDA) Treatment: PDA was performed using a rapid thermal annealing system (ECOPIA RTP-1200). The samples were heated to 800 ℃ for 10 min with a ramp-up rate of 30 ℃/s in a nitrogen atmosphere.

Structural and Chemical Analysis: The surface morphology was determined in standard tapping mode with a Si tip radius of <10 nm using a Bruker Dimension ICON AFM system. The XRD spectra were collected at 0.02° step size in the 2θ range of 20° to 90° using Bruker AXS (D8 Advance) powder patterns. The samples for TEM measurements were prepared by focused ion beam (FEI Scios) lift-out and polishing, followed by low-energy argon ion milling. The TEM and STEM data were acquired with a probe-aberration-corrected JEOL ARM 200F operated at 200 kV. The STEM-EELS spectrum images (SI) were recorded using a Gatan GIF Quantum

ER system with 1 eV/channel energy dispersion. The low-loss and core-loss were simultaneously recorded to allow advanced post-processing of data (energy-drift correction and plural scattering correction). The principal component analysis was applied to denoise the core-loss SI before extracting quantitative elemental maps. The XPS spectra were acquired using a Thermo Fisher ESCALAB Xi^+ X-ray photoelectron spectrometer equipped with a monochromatic Al Kα X-ray source (1486.7 eV). A low-energy electron flood gun (0–5 eV) was utilized for charge neutralization during the measurements. The deconvolution of all the peaks was performed using CasaXPS program, and the peak fitting was performed using Gaussian–Lorentzian peak shape with Shirley-type background subtraction. Prior to the XPS experiment, the samples were exposed to air for approximately 2 h owing to the annealing treatment. The AlBN films were cleaned by Ar^+ sputtering to remove the surface pollutants. All binding energies reported in this study were relative to the C 1s peak at a binding energy of 284.8 eV.

Fabrication of Au/AlBN/n^{++}GaN Capacitors: Two simple Au/AlBN/n^{++}GaN capacitors were fabricated to test the electrical properties of the as-deposited and 800 °C PDA films. The ohmic contacts were formed by electron beam evaporation with Ti/Al/Ni/Au (20/130/50/150 nm) metal stacks followed by rapid thermal annealing at 890 °C for 30 s in a nitrogen atmosphere. Subsequently, the AlBN films were deposited on n^{++}GaN surfaces and one of them was subsequently annealed. Finally, an electron beam system (ULVAC ei-5z) evaporated the Ni/Au (50/150 nm) circular top electrodes of 200 μm-diameter through metal masks. The capacitor schematic is illustrated in Figure 5a.

Characterization of Capacitors: The current density–electric field (J–E) and C–V characteristics of Au/AlBN/n^{++}GaN capacitors were measured by a Keithley 4200-SCS/F parameter analyzer system and SUSS PM8 high precision probe station. In J–E tests, a positive voltage was applied to the Au electrode on the films, and the applied voltage was swept from 0 to 14 V. The C–V measurements were conducted in the voltage range from -15 to 2 V with an

AC drive voltage of 30 mV.

Supporting Information
Supporting Information is available from the Wiley Online Library or from the author.

Acknowledgements
This work was supported by the National Natural Science Foundation of China (Grant 61801449), National Natural Science Foundation of China Joint Fund Project (U1830112), and Science and Technology Project of Jiangsu Province (BE2018006-3). Y. Lu acknowledges the support of the French National Research Agency (ANR) FEOrgSpin (Grants No. ANR-18-CE24-0017-01), in addition to the ICEEL BlueSpinLED and SHATIPN projects. The authors are grateful for the technical support for Nano-X from the Suzhou Institute of Nano-Tech and Nano-Bionics, Chinese Academy of Sciences (SINANO).

Received: ((will be filled in by the editorial staff))
Revised: ((will be filled in by the editorial staff))
Published online: ((will be filled in by the editorial staff))

References

[1] D. A. Muller, T. Sorsch, S. Moccio, F. H. Baumann, K. Evans-Lutterodt, G. Timp, *Nature* **1999**, *399*, 758.

[2] F. Palumbo, C. Wen, S. Lombardo, S. Pazos, F. Aguirre, M. Eizenberg, F. Hui, M. Lanza, *Adv. Funct. Mater.* **2019**, *30*, 1900657.

[3] M. Xiao, Y. Ma, K. Liu, K. Cheng, Y. Zhang, *IEEE Electron Device Lett.* **2021**, *42*, 808.

[4] M. Cwiklinski, P. Bruckner, S. Leone, S. Krause, C. Friesicke, H. Massler, R. Quay, O. Ambacher, in *2020 IEEE/MTT-S International Microwave Symposium (IMS)*, IEEE, Los Angeles, CA 2020, pp. 1117-1120.

[5] J. He, W.-C. Cheng, Q. Wang, K. Cheng, H. Yu, Y. Chai, *Adv. Electron. Mater.* **2021**, *7*, 2001045.

[6] J. Lee, J. M. Lee, H. Oh, C. Kim, J. Kim, D. H. Kim, B. Shong, T. J. Park, W. H. Kim, *Adv. Funct. Mater.* **2021**, *31*, 2102556.

[7] Z. Zhang, G. Yu, X. Zhang, X. Deng, S. Li, Y. Fan, S. Sun, L. Song, S. Tan, D. Wu, W. Li, W. Huang, K. Fu, Y. Cai, Q. Sun, B. Zhang, *IEEE Trans. Electron Devices* **2016**, *63*, 731.

[8] L. Shen, D. Zhang, X. Cheng, L. Zheng, D. Xu, Q. Wang, J. Li, D. Cao, Y. Yu, *IEEE Electron Device Lett.* **2017**, *38*, 596.

[9] C. Liu, E. F. Chor, L. S. Tan, *Appl. Phys. Lett.* **2006**, *88*, 173504.

[10] J. K. Gillespie, R. C. Fitch, J. Sewell, R. Dettmer, G. D. Via, A. Crespo, T. J. Jenkins, B. Luo, R. Mehandru, J. Kim, F. Ren, B. P. Gila, A. H. Onstine, C. R. Abernathy, S. J. Pearton, *IEEE Electron Device Lett.* **2002**, *23*, 505.

[11] B. S. Kang, H. T. Wang, F. Ren, B. P. Gila, C. R. Abernathy, S. J. Pearton, J. W. Johnson, P. Rajagopal, J. C. Roberts, E. L. Piner, K. J. Linthicum, *Appl. Phys. Lett.* **2007**, *91*, 012110.

[12] N. V. Nguyen, C. A. Richter, Y. J. Cho, G. B. Alers, L. A. Stirling, *Appl. Phys. Lett.* **2000**, *77*, 3012.

[13] Y.-C. Byun, J.-G. Lee, X. Meng, J. S. Lee, A. T. Lucero, S. J. Kim, C. D. Young, M. J. Kim, J. Kim, *Appl. Phys. Lett.* **2017**, *111*, 082905.

[14] Q. A. Vu, S. Fan, S. H. Lee, M.-K. Joo, W. J. Yu, Y. H. Lee, *2D Mater.* **2018**, *5*, 031001.

[15] N. R. Glavin, C. Muratore, M. L. Jespersen, J. Hu, P. T. Hagerty, A. M. Hilton, A. T. Blake, C. A. Grabowski, M. F. Durstock, M. E. McConney, D. M. Hilgefort, T. S. Fisher, A. A. Voevodin, *Adv. Funct. Mater.* **2016**, *26*, 2640.

[16] C. Yang, X. Luo, A. Zhang, S. Deng, D. Ouyang, F. Peng, J. Wei, B. Zhang, Z. Li, *IEEE Trans. Electron Devices* **2018**, *65*, 5203.

[17] H. Kim, H. J. Yun, S. Choi, B. J. Choi, *Trans. Electr. Electron. Mater.* **2020**, *21*, 621.

[18] D. Ceresoli, D. Vanderbilt, *Phys. Rev. B* **2006**, *74*, 125108.

[19] S. Toyoda, T. Shinohara, H. Kumigashira, M. Oshima, Y. Kato, *Appl. Phys. Lett.* **2012**, *101*, 231607.

[20] H. Cakmak, M. Ozturk, E. Ozbay, B. Imer, *IEEE Trans. Electron Devices* **2021**, *68*, 1006.

[21] Y. Gu, Y. Zhang, B. Hua, X. Ni, Q. Fan, X. Gu, *J. Electron. Mater.* **2021**, *50*, 4239.

[22] Y.-F. Wu, A. Saxler, M. Moore, R. P. Smith, S. Sheppard, P. M. Chavarkar, T. Wisleder, U. K. Mishra, P. Parikh, *IEEE Electron Device Lett.* **2004**, *25*, 117.

[23] Y. Gu, Y. Zhang, B. Hua, X. Ni, Q. Fan, X. Gu, *J. Electron. Mater.* **2021**, *50*, 4239.

[24] V. Iglesias, M. Porti, M. Nafria, X. Aymerich, P. Dudek, G. Bersuker, *J. Vac. Sci. Technol. B* **2011**, *29*, 01AB02.

[25] G. Cassabois, P. Valvin, B. Gil, *Nat. Photonics* **2016**, *10*, 262.

[26] J.-G. Ahn, G. Yeo, Y. Han, Y. Park, J. W. Hong, H. Lim, *ACS Appl. Mater. Interfaces* **2021**, *13*, 42176.

[27] L. Wang, X. Xu, L. Zhang, R. Qiao, M. Wu, Z. Wang, S. Zhang, J. Liang, Z. Zhang, Z. Zhang, W. Chen, X. Xie, J. Zong, Y. Shan, Y. Guo, M. Willinger, H. Wu, Q. Li, W. Wang, P. Gao, S. Wu, Y. Zhang, Y. Jiang, D. Yu, E. Wang, X. Bai, Z.-J. Wang, F. Ding, K. Liu, *Nature* **2019**, *570*, 91.

[28] W. Wang, W. Yang, Z. Liu, H. Wang, L. Wen, G. Li, *Sci. Rep.* **2015**, *5*, 11480.

[29] C. Cibert, P. Dutheil, C. Champeaux, O. Masson, G. Trolliard, F. Tétard, A. Catherinot, *Appl. Phys. Lett.* **2010**, *97*, 251906.

[30] F. Engelmark, J. Westlinder, G. F. Iriarte, I. V. Katardjiev, J. Olsson, *IEEE Trans. Electron Devices* **2003**, *50*, 1214.

[31] J. H. Choi, Y. Mao, J. P. Chang, *Mater. Sci. Eng. R: Rep.* **2011**, *72*, 97.

[32] Y. B. Lee, I.-K. Oh, E. N. Cho, P. Moon, H. Kim, I. Yun, *Appl. Surf. Sci.* **2015**, *349*, 757.

[33] S.-K. Yang, S. Mazumder, Z.-G. Wu, Y.-H. Wang, *Materials* **2021**, *14*, 1534.

[34] J. Robertson, R. M. Wallace, *Mat. Sci. Eng. R: Rep.* **2015**, *88*, 1.

[35] H. Sun, C. G. T. Castanedo, K. Liu, K.-H. Li, W. Guo, R. Lin, X. Liu, J. Li, X. Li, *Appl. Phys. Lett.* **2017**, *111*, 162105.

[36] Y. Lu, J. C. Le Breton, P. Turban, B. Lépine, P. Schieffer, G. Jézéquel, *Appl. Phys. Lett.* **2006**, *88*, 042108.

[37] T. Schultz, M. Kneiss, P. Storm, D. Splith, H. von Wenckstern, M. Grundmann, N. Koch, *ACS Appl. Mater. Interfaces* **2020**, *12*, 8879.

[38] D. Sánchez-Ahumada, L. J. Verastica-Ward, M. Orozco, D. Vargas-Hernández, A. Castro-Beltrán, R. Ramirez-Bon, C. G. Alvarado-Beltrán, *Prog. Org. Coat.* **2021**, *154*, 106188.

[39] M. X. Li, M. W. Yao, W. B. Gao, Z. Su, X. Yao, *Electrochim. Acta* **2019**, *313*, 20.

[40] S. Pawar, K. Singh, S. Sharma, A. Pandey, S. Dutta, D. Kaur, *Mater. Chem. Phys.* **2018**, *219*, 74.

[41] S. Hong, C.-S. Lee, M.-H. Lee, Y. Lee, K. Y. Ma, G. Kim, S. I. Yoon, K. Ihm, K.-J. Kim, T. J. Shin, S. W. Kim, E.-C. Jeon, H. Jeon, J.-Y. Kim, H.-I. Lee, Z. Lee, A. Antidormi, S. Roche, M. Chhowalla, H.-J. Shin, H. S. Shin, *Nature* **2020**, *582*, 511.

[42] L. Li, X. M. Chen, *Nature* **2021**, *590*, E6.